PNAS RESEARCH ARTICLE | EARTH, ATMOSPHERIC, AND PLANETARY SCIENCES

Probing multiscale dissolution dynamics in natural rocks through microfluidics and compositional analysis

Bowen Ling[a,1], Mo Sodwatana[a], Arjun Kohli[a], Cynthia M. Ross[a], Adam Jew[b], Anthony R. Kovscek[a], and Ilenia Battiato[a,2]

Edited by Howard Stone, Princeton University, Princeton, NJ; received December 13, 2021; accepted June 6, 2022

Mineral dissolution significantly impacts many geological systems. Carbon released by diagenesis, carbon sequestration, and acid injection are examples where geochemical reactions, fluid flow, and solute transport are strongly coupled. The complexity in these systems involves interplay between various mechanisms that operate at timescales ranging from microseconds to years. Current experimental techniques characterize dissolution processes using static images that are acquired with long measurement times and/or low spatial resolution. These limitations prevent direct observation of how dissolution reactions progress within an intact rock with spatially heterogeneous mineralogy and morphology. We utilize microfluidic cells embedded with thin rock samples to visualize dissolution with significant temporal resolution (100 ms) in a large observation window (3 × 3 mm). We injected acidic fluid into eight shale samples ranging from 8 to 86 wt % carbonate. The pre- and postreaction microstructures are characterized at the scale of pores (0.1 to 1 μm) and fractures (1 to 1,000 μm). We observe that nonreactive particle exposure, fracture morphology, and loss of rock strength are strongly dependent on both the relative volume of reactive grains and their distribution. Time-resolved images of the rock unveil the spatiotemporal dynamics of dissolution, including two-phase flow effects in real time and illustrate the changes in the fracture interface across the range of compositions. Moreover, the dynamical data provide an approach for characterizing reactivity parameters of natural heterogeneous samples when porous media effects are not negligible. The platform and workflow provide real-time characterization of geochemical reactions and inform various subsurface engineering processes.

dissolution | microfluidics | geochemistry | mineralogy

A number of studies indicate that carbonate dissolution from both natural and anthropogenic causes contributes to global carbon emissions (1, 2), cap rock destabilization at CO_2 sequestration sites (3), mobilization of heavy metal elements in groundwater (4), fracture collapse within reservoirs (5), and heavy metal bioavailability in soils (6). Dissolution in geologic systems is typically comprised of a chain of geochemical reactions controlled by solid and fluid interactions, fracture and porosity evolution, and reactive solute transport (7). As reactions progress, the fluid chemistry is impacted by flow and reactive solute availability. In turn, the flow and concentration fields are altered as the fracture and pore geometry evolve via dissolution that is controlled by the mineralogy and heterogeneity of the rock (8, 9). Controlling and optimizing various subsurface processes (8–14) require an experimental platform that captures both the real-time dynamics of dissolution and provides insight into the coupling and feedbacks between different physical processes. Yet, the inherent multiphysics nature of reactive transport in rocks is only one of the challenging aspects of studying such systems by direct observation. These strongly coupled and highly localized physical phenomena often occur on vastly different characteristic spatial and temporal scales. For example, the spatial scales associated with advective mass transport in fractures may be much larger than the characteristic scale of reactive mass transport at the rock surface. Such a disparity in scales requires that the experimental techniques used to probe the dynamic feedbacks of reactive transport in natural samples have both high temporal and spatial resolution and maintain a significant field of view to capture both 1) physicochemical processes over multiple spatial and temporal scales as well as 2) the sample's mineralogical heterogeneity. Achieving high temporal resolution and large fields of view during dissolution processes, in combination with compositional information, is critical to investigate a number of open scientific questions in the context of rock weathering kinetics. What is the impact of spatial heterogeneity and reactive surface accessibility on reaction rates and porosity–surface area correlations in real rock samples? Can these effects be quantified in laboratory setups and incorporated in reactive transport models? Although dynamic models for porosity and surface evolution are critical to assess reactivity, they are incredibly difficult to constrain, particularly in natural heterogeneous samples, where porous media effects may be major (15–17).

Significance

Dissolution reactions are ubiquitous in many geological systems. The interactions between rocks and acidic fluids are complex, dynamic, and dependent on rock properties and morphology. Physical processes with vastly different time and spatial scales may occur simultaneously, presenting challenges for current experimental techniques. Here, we propose a platform for probing dissolution dynamics, in which natural samples are embedded in microfluidic cells and are imaged combining high-speed camera data acquisition techniques, scanning electron microscopy, and energy-dispersive spectroscopy to characterize dissolution processes at very high spatial (0.1 to 1 μm) and temporal (0.1 s) resolutions over large fields of view (millimeters). Static and dynamic images provide a direct mechanistic understanding of dissolution over a range of temporal and spatial scales.

Author contributions: B.L., A.R.K., and I.B. designed research; B.L., M.S., A.K., C.M.R., and A.J. performed research; A.K., C.M.R., and A.J. contributed new reagents/analytic tools; B.L., M.S., C.M.R., and I.B. analyzed data; and B.L., C.M.R., A.R.K., and I.B. wrote the paper.

The authors declare no competing interest.

This article is a PNAS Direct Submission.

[1]Present address: Institute of Mechanics, Chinese Academy of Sciences, Beijing, China, 100190.

[2]To whom correspondence may be addressed. Email: ibattiat@stanford.edu.

This article contains supporting information online at https://www.pnas.org/lookup/suppl/doi:10.1073/pnas.2122520119/-/DCSupplemental.

Published August 3, 2022.

Generally, a trade-off exists between spatial and temporal resolution in dissolution experiments. Nonoptical experimental techniques (e.g., X-ray microtomography [μCT] and scanning electron microscopy [SEM]) provide structural and mineral information at submicrometer scales (18–20); however, these methods each have drawbacks with respect to characterizing dynamically in situ dissolution because of long acquisition times for μCT (21) and the need to keep samples under vacuum conditions for SEM-based applications (22). Dissolution reactions can occur within microseconds after the reactive fluid reaches soluble minerals and can continue interacting with the minerals for days. Documenting dissolution dynamics of real rocks at relevant scales requires an in situ platform with large temporal resolution and significant fields of view. Yet, high-resolution imaging is restricted by sample size and/or the camera's field of view.

Microfluidic devices have been rapidly evolving to meet growing experimental needs and can be imaged using cameras with fast frame rates (23–26). Consequently, applications of microfluidic devices provide opportunities to study dissolution reaction mechanisms and the strong influence brought by fluid flow. For example, Song et al. (26) designed a calcite-functionalized microfluidic device to study multiphase reactive systems at the pore scale. Soulaine et al. (23) engineered a calcite grain–bearing microfluidic cell within which the dissolution process is recorded at high temporal resolution. Dynamical dissolution data show the interaction between flow and reactive transport while providing experimental benchmarks for theoretical and numerical model development. Yet, geological formations exhibit significant physicochemical heterogeneity, whose complexity cannot be captured by synthesized materials (e.g., $CaCO_3$). Natural samples are usually highly heterogeneous in composition (27–29), fracture morphology (30–32), and mineral distribution (23, 33, 34). Moreover, as dissolution reactions generate additional phases in the fluid (e.g., gases), the hydrodynamics of these systems depend strongly on the surface properties, such as the wettability and the topology of mineral surfaces, which synthetic materials do not replicate.

Recent studies that integrate natural samples into microfluidics have improved our understanding of the fundamentals of fluid–solid interactions and reactive transport in subsurface environments (35–38). Deng et al. (36) show an in operando synchrotron system based on a micromodel coupled with real rock, in which the reaction is recorded with spatial resolution of 1.3 μm and temporal resolution of 15 min/frame. This study shows the significant pore space change brought by dissolution reactions. However, such temporal resolution is not sufficient to study the real-time interplay between dissolution reactions and morphological changes of the rock associated with its mineralogical heterogeneity and fluid flow.

To address these limitations, we designed a sample-embedded microfluidic cell that can be imaged both in situ at high temporal resolution using optical imaging and ex situ at high spatial resolution using electron microscopy. The combination of such techniques allows us to study multiscale multiphysics dynamic dissolution processes and their interplay with flow at relevant temporal scales and large fields of view (millimeter scale) while mapping the rock's chemical heterogeneity at a much finer scale (0.1-μm scale). This study incorporates correlative optical and SEM-based energy-dispersive spectroscopy (EDS) elemental maps on the same natural sample before and after dissolution reactions. By combining dynamic optical imaging and high-resolution SEM imaging and spectroscopy, we show that dissolution results from a tight coupling between fracture topology evolution, reaction rate heterogeneity induced by local chemical composition and mediated by fracture-scale flow, and nonreactive particle exposure. Specifically, direct backscattered electron (SEM-BSE) imaging postmortem visualizations of the reacted sample allow us to identify distinct features of the reacted interface across shale samples with carbonate content ranging between 8 and 86 wt %. Our study demonstrates how the coupling between flow and reactive transport during acidification of shale samples with different carbonate contents is strongly controlled by the sample's chemical composition and the characteristic length scale of the physicochemical heterogeneity (i.e., carbonate particle size) at the flow rate investigated. Concurrent analysis of high–temporal resolution images and chemical composition allows one to track locally the impact of reactive transport and dissolution across multiple scales and visualize its effects on the topological features of the altered layer. Finally, via the high–temporal resolution results, dynamical relationships between fracture volume and mineral surface area can be determined as a function of carbonate content and distribution; such correlations are critical to assess reactivity in reactive transport models.

Materials and Methods

Shale Samples Description and Preparation. In this study, we employ eight shale samples with carbonate content ranging from 8 to 86 wt %: three samples from the Marcellus carbonate-rich shale (denoted as Marcellus, Marcellus [2], and Marcellus [3]) and five samples from the Wolfcamp shale (WC 2-5H, WC 2-5H [2], WC 2-5H [3], WC 6-1H, and WC 3-2V). The composition of each sample is described in the ternary diagram in Fig. 1*A*. The same name indicates that the samples are from the same core, while the number in brackets indicates that the experiment is replicated across different samples (replicas) with the same composition. The shale samples contain reactive carbonate minerals, such as calcite ($CaCO_3$) and dolomite [$CaMg(CO_3)_2$], that occur as fossils, individual crystals, discrete grains, and interlocking crystalline networks. In carbonate-rich samples, silicates (SiO_4-bearing minerals, such as quartz) as well as other minerals are distributed in a carbonate matrix. These noncarbonate minerals may be concentrated in horizontal laminations and other structures. In carbonate-poor samples, carbonate minerals occur as small particles that are spread sporadically throughout the matrix and, in some cases, may be isolated to particular structures, such as horizontal laminations. Although we focus on shales with variable compositions, small initial porosity, and fine grain size, the approach is directly applicable to other sample types. Once collected, rock samples are first polished to the desired thickness ($\sim$200 μm) and cut to size 3 × 3 mm. Then, two perpendicular grooves are scored into the sample, and finally, the entire piece is quartered into four pieces of approximate size $L \sim 0.75$ mm; L is large enough to capture the chemical and physical heterogeneity, whose characteristic length scale is ℓ. For the carbonate-rich sample (Marcellus), $\ell \gg L$ (with ℓ the size of carbonate particles); $\ell \approx L$ for the sample with intermediate carbonate content (WC 2-5H), and $\ell \ll L$ for the carbonate-poor samples (WC 6-1H and WC 3-2V).

Pre- and Postreaction Characterization and Sample-Embedded Microfluidic Cell Fabrication. Once the sample preparation is completed, each sample is characterized prereaction using SEM-BSE and EDS for elemental distribution and mineral identification (TFS Apreo S LoVac with Bruker Quantax 6|60 EDS detector and Esprit 2.2 software). Once prereaction characterization is completed, the left side of the sample is inserted in the flow cell, molded from polydimethylsiloxane (PDMS) using a silicon wafer mold, and aligned with the flow chamber wall such that the sample pieces create two intersecting fractures, the fracture entrance is aligned with the microfluidic inlet, and the width of the inlet is 200 μm. To close and seal the chamber, we spin coat a glass slide with PDMS and bond it to the flow cell. With the top and bottom surfaces of the sample sealed by PDMS, the fluid can only travel through the fractures. The microfluidic device is a quasi-two-dimensional (quasi-2D) chip with a $\sim$200-μm rock sample embedded inside a central flow chamber (Fig. 1*B*). This microfluidic device allows visualization through the glass slide and captures the quasi-2D surface variation of the fractures during the dissolution experiments as detailed in the following section. After the dissolution experiment, the microfluidic chip is cut open, and the sample is moved to a glass slide for postreaction SEM-BSE and EDS characterization. A flowchart of the experimental protocol is provided in Fig. 1*C*.

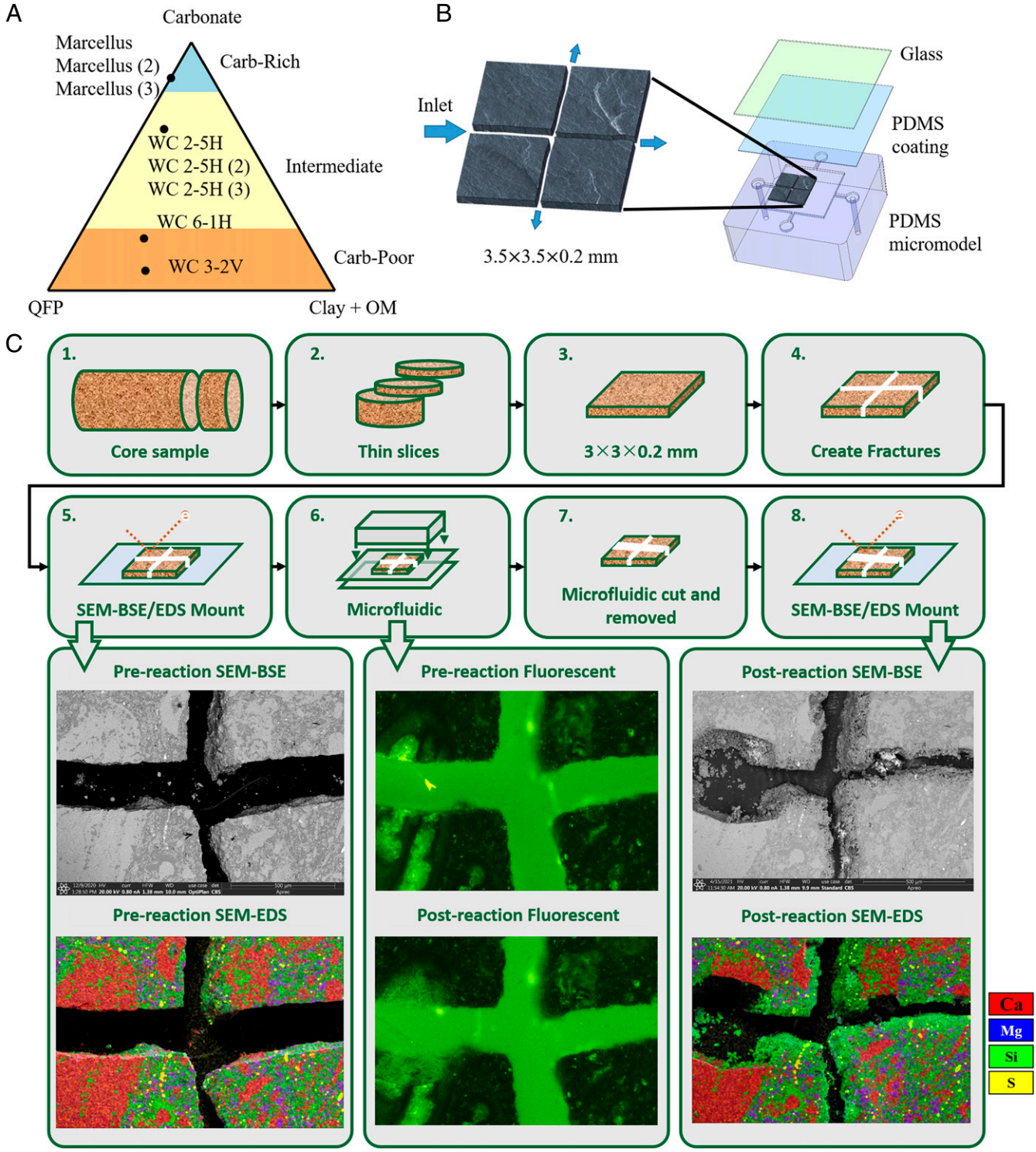

Fig. 1. (*A*) Compositional ternary plot of the four study samples and their replicas (*SI Appendix*, Table S1). The Marcellus sample is carbonate rich. The clay-rich Wolfcamp sample, WC 3-2V, occurs at the other end of the carbonate spectrum. Two other Wolfcamp samples have compositions between these two endmembers. OM, organic matter; QFP, quartz, feldspar, and pyrite. (*B*) Sample-embedded microfluidic cell construction. Rock samples are polished into thin wafers and quartered. The pieces are placed in the flow chamber and aligned with the inlet to simulate two intersecting fractures. The glass cover used for visul access is coated with PDMS and bonded to the flow chamber. (*C*) Flowchart of the experimental protocol. The sample preparation starts with thin slices of core samples (*C*, *1* and *C*, *2*); each piece is ground and polished to a thickness of 0.2 mm and cut to 3 × 3 mm (*C*, *3*). We score and break the sample into four pieces (*C*, *4*). These four pieces are placed on a glass slide for prereaction SEM-BSE and EDS scanning (*C*, *5*). Afterward, the four pieces are placed on a PDMS-coated glass slide, configured to form intersecting fractures, aligned with the inlet to create a 0.2-mm fracture, and sealed in the microfluidic chip. The fluorescent microscopy and dynamic dissolution measurements are conducted (*C*, *6*). After the dissolution experiment, the microfluidic cell is cut open (*C*, *7*), and the postreaction sample (four pieces) is mounted for postreaction characterization via SEM-BSE and EDS (*C*, *8*).

Microfluidic Dissolution Experiments. Dynamic flow and reactive transport experiments are performed by adapting fluorescent microscopy visualization techniques from previous studies (39–41) and following the same experimental protocol for all the samples. We first saturate the fractured samples and sample cell with deionized (DI) water. The saturated chip is then placed on a motorized stage and viewed using an inverted microscope (Ti-E; Nikon Instruments Inc.). Fluorescent dye ALEXA-488 (ThermoFisher Scientific, Inc.) is injected before and after dissolution to enhance the boundary contrast between the fracture space

and the solid matrix. A compatible filter cube (C-FL GFP; Nikon Instruments Inc.) restricts the spectrum to green/blue light only. Acid solution (1% HCl) is injected at a flow rate of $Q = 1{,}000$ μL/h for 3 min, and the valves switch immediately to DI-water injection when the acid injection is completed. This flow rate corresponds to an average velocity $U \sim 6.94 \times 10^{-2}$ m/s inside the fracture (at the inlet) and a Péclet number $Pe = LU/D \sim 149.1$, where $L = 200$ μm and $D = 9.31 \times 10^{-9}$ m^2/s is the diffusion coefficient of H^+ in water. The Damköhler number is $Da = \alpha_{H+} L^2/D = 1.91$, where $\alpha_{H+} = 0.456$ s^{-1} is the reaction rate constant of H^+ (42). The entire injection process is recorded by a high-speed camera (Hamamatsu Flash LT Monochrome; Hamamatsu) that is connected to the inverted microscope, with the recording set to capture ∼10 images or frames per second with the field of view (3 × 3 mm). For the samples in this study, the minerals dissolved by HCl are mostly calcite and some dolomite. CO_2 gas is released during the experiments and, in most cases, can be imaged. The reaction between calcite and HCl is

$$CaCO_3(s) + 2HCl(aq) \rightarrow CaCl_2(aq) + CO_2(g) + H_2O(aq),$$

where the CO_2 may dissolve to form carbonic acid, H_2CO_3, that may dissociate into HCO_3^-, CO_3^{2-}, and H^+. Of course, the amount of H_2CO_3 formed in solution depends on pressure and temperature. Further information about sample composition, rock preparation, microfluidic cell construction, experimental setup, and protocols is provided in the *SI Appendix*.

Results and Discussion

Dynamic Imaging Results. Dynamic dissolution images at 120- to 130-s time intervals for four of the eight experiments are shown in Fig. 2. Fig. 2 includes images for samples with high (Marcellus), intermediate (WC 2-5H [2] and WC 2-5H [3]), and low (WC 3-2V) carbonate content. Select optical images collected before, during, and after dissoluton for all samples are available in *SI Appendix*, Figs. S11–S17. The original images are provided in the Stanford Digital Repository. All of the initial experiments for each sample have corresponding pre- and postreaction SEM-BSE and EDS data.

For the Marcellus (with $\ell \gg L$) and the WC 2-5H (2) and WC 2-5H (3) samples (with $\ell \sim L$), substantial changes in the width, shape, and tortuosity of the fractures are caused by dissolution and imaged in real time. However, while the fractures widen uniformly and the roughness of the fracture surfaces remains similar before and after dissolution in the Marcellus sample, in the WC 2-5H samples the fractures widen substantially and heterogeneously corresponding to the occurrence of large calcite fossils, and the surface roughness abruptly changes after dissolution (*SI Appendix*, Figs. S8 and S9).

Optical images of WC 2-5H (2) and WC 2-5H (3) samples reveal strong mineral heterogeneity, which are characterized using SEM-BSE and EDS static images in the following section. Dynamic imaging of all WC 2-5H experiments shows preferential reaction patterns in which large calcite regions are selectively dissolved, resulting in the generation of large bubbles in these areas. The silicate-rich regions remain comparatively unaffected (Fig. 2 and *SI Appendix*, Figs. S14–S16). This is most apparent in the before and after fluorescent images in *SI Appendix*, Fig. S9. In comparison, the carbonate-poor sample, WC 3-2V, does not show any visual structural/topological change at this scale. Note

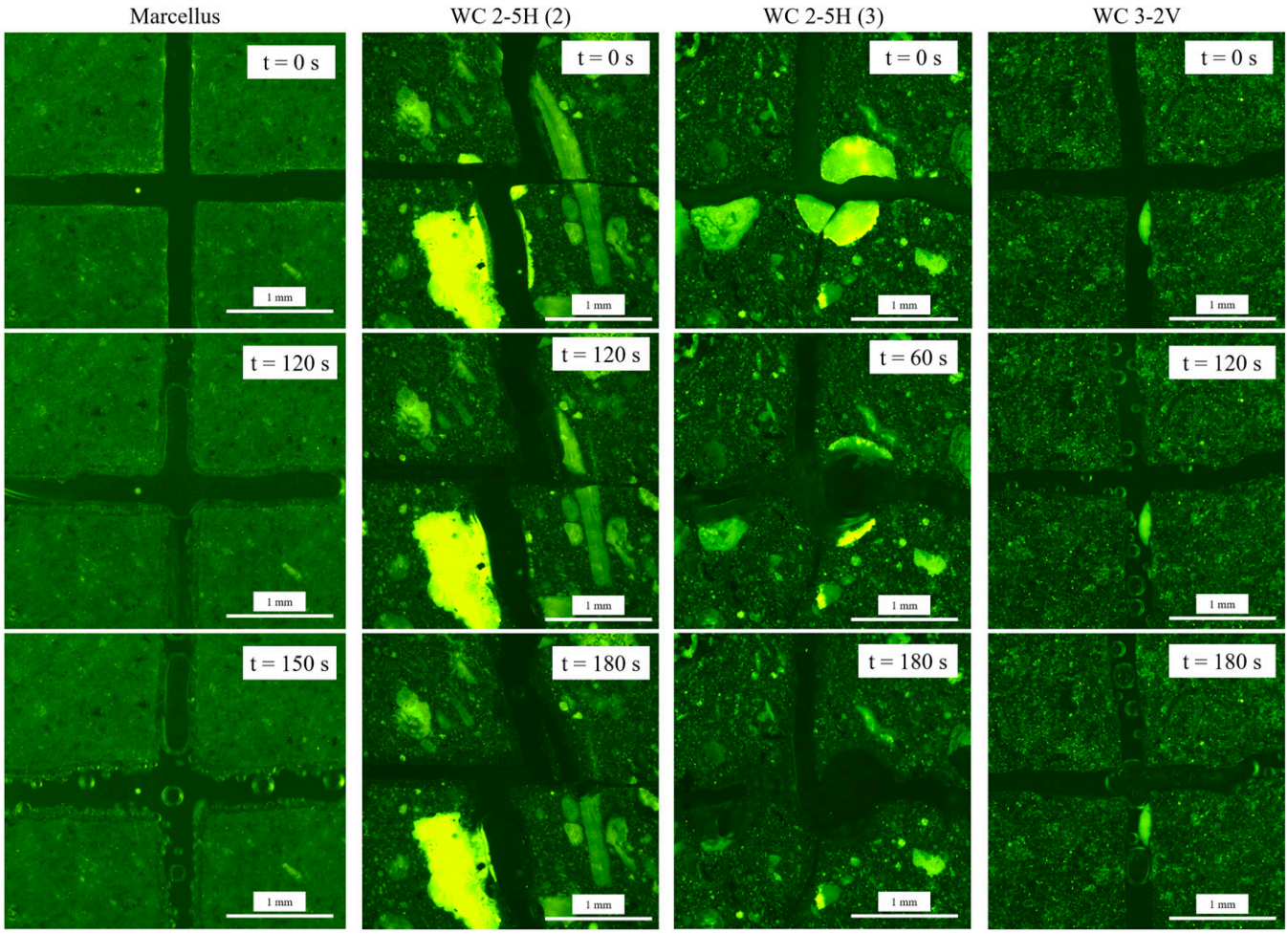

Fig. 2. Dynamic dissolution images for three different samples at different time instances (image width = 3 mm).

that although dissolution of isolated carbonate grains within the silicate regions adjacent to the fracture wall cannot be resolved at this magnification, small bubbles are observed in these areas, suggesting that dissolution may be occurring (Fig. 2). This observation is consistent with the pre- and postreaction SEM-BSE images, which do show dissolution of these isolated grains as discussed in the *Static Results* section. Overall, the high-speed large field of view optical imaging allows us to visualize dynamically changes in the aperture and macroscopic features of the fractures for samples with greater carbonate content that are controlled by the coupling between reaction, heterogeneity, and advective transport. To analyze quantitatively these images, we track the evolution of integral geometric quantities (fracture volume and interface length) as reaction progresses. Specifically, we define the normalized fracture volume (Ψ) as

$$\Psi(t) = \frac{V(t)}{V_0},$$

where $V(t)$ is the fracture volume at each time interval and V_0 is the total volume of the sample, $V_0 = 3 \times 3 \times 0.2 = 1.8$ mm^3. Because the fractured sample is quasi-2D, with the image being the focusing plane, we define a normalized solid–fracture interface length $\Gamma(t)$ rather than an interface area as

$$\Gamma(t) = \frac{L(t)}{L_0},$$

where $L(t)$ is the interface length at each time instance and L_0 is the interface length at time $t = 0$ s. This quantity provides information about the evolution of interfacial length during reactions. When $\Gamma(t) > 1$ for $t > t_0$, the new interface is generated as a result of the dissolution process. If $\Gamma(t) < 1$ for $t > t_0$, the interface length is decreasing (i.e., the interface is becoming smoother). If $\Gamma(t) \approx 1$ for $t > t_0$, then the fracture interface length remains approximately constant during dissolution. The area (used to calculate the volume as fracture area multiplied by the depth [0.2 mm]) and interface lengths are measured using image segmentation and the edge detection tool in ImageJ (Fig. 3*A*). In Fig. 3*B*, we plot the calculated $\Gamma(t) - \Psi(t)$ correlations as time progresses for all samples and their replicas (symbols connected by solid lines). Fig. 3*B* shows that $\Gamma(t)$ and $\Psi(t)$ can be positively correlated, negatively correlated, or remain constant as time evolves [i.e., $(\Gamma(t), \Psi(t)) = (\Gamma(t_0), \Psi(t_0))$], depending on the carbonate content of the sample (or alternatively, the characteristic length scale of the carbonate heterogeneity). Specifically, all Marcellus samples ($\ell \gg L$) exhibit a negative correlation between Γ and Ψ (i.e., $d\Gamma/d\Psi < 0$), with Γ decreasing as fracture volume Ψ increases during dissolution ($t > t_0$). Alternatively, the Wolfcamp samples with intermediate carbonate content ($\ell \sim L$) have a positive correlation between Γ and Ψ (i.e., $d\Gamma/d\Psi > 0$), with Γ increasing as fracture volume Ψ increases during dissolution ($t > t_0$). The changes in normalized surface length for the high to medium carbonate content samples can be significant and in the $\pm 20\%$ range. Fracture volume can also significantly change with variations up to 25 to 100%. The slopes of $\Gamma - \Psi$ curves for the Marcellus and WC2-5H samples in Fig. 3*B* are similar for each sample set, indicating that the reaction rate of calcite is approximately the same among samples with similar carbonate content; the dissolution reaction rate is not limited by reactive minerals in the Marcellus samples (i.e., the timescale of the reaction is dominated by the reaction rate of pure calcite). Because mass transport is controlled by advection at high Peclet numbers, the greatest discrepancies in each class are caused by heterogeneities in the spatial distribution of reactive minerals (e.g., WC 2-5H curves, Fig. 3*B*) and their accessibility to the connected pore space. Starkly different behavior is exhibited by

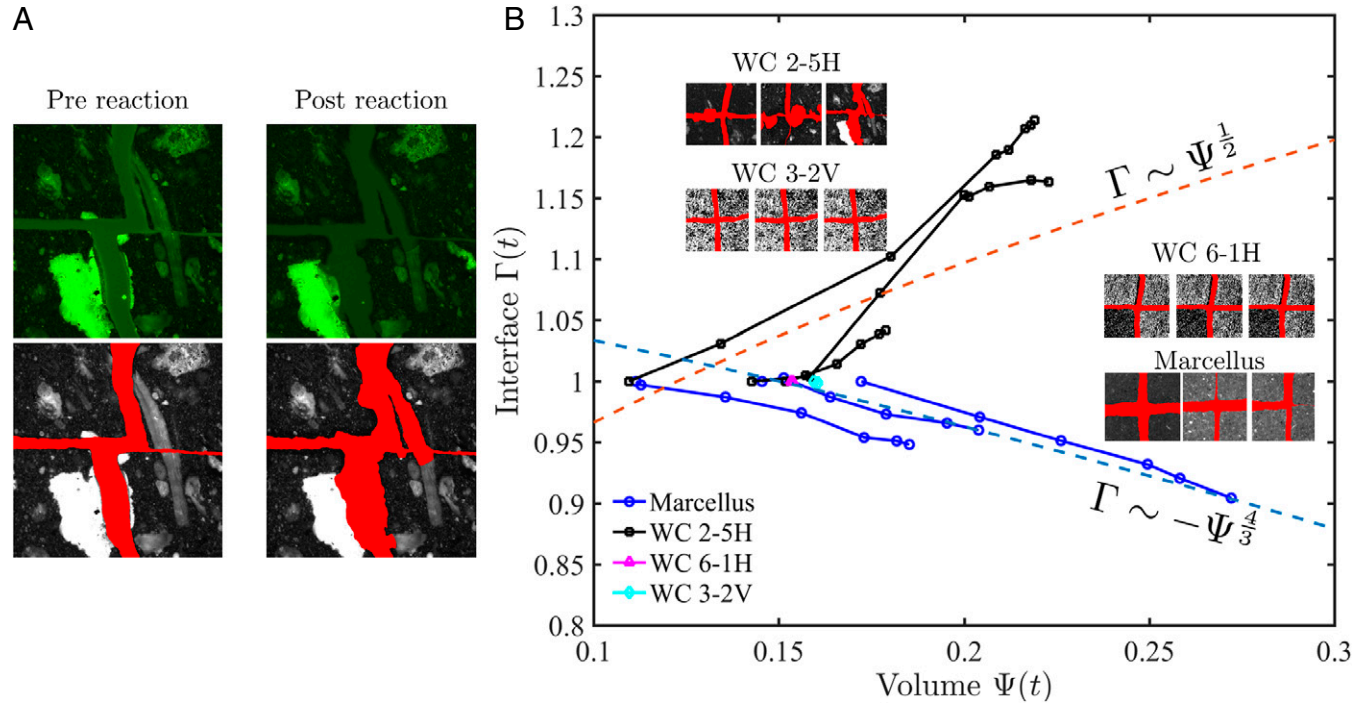

Fig. 3. Image characterization of fracture porosity and its evolution. (*A*) Example fluorescent images of dye-filled fractures pre- and postreaction (WC 2-5H [2], *Top Row*). Fracture space is segmented from the surrounding rock (as shown in red) in processed fluorescent images (*Bottom Row*). The segmented region is used to calculate normalized fluid volume (Ψ) and the interface fracture length, Γ, with time. (*B*) Evolution of fracture volume and solid–fracture interface lengths with reaction time. Results of three replicate experiments for WC 2-5H and Marcellus are plotted using the corresponding Ψ and Γ at each time interval. The dashed blue line shows the scaling of Eq. **1**, specifically $\Gamma = 1.08 - \Psi^{4/3}$. The dashed red line is $\Gamma = 0.65 + \Psi^{1/2}$. Example processed images are included as insets. Additional images are in *SI Appendix*, Figs. S8–S17. The original images are provided in the Stanford Digital Repository (see *Data Availability*).

the carbonate-poor samples (WC 6-1H and WC 3-2V), for which no change in either fracture surface area or fracture volume can be detected at this scale (millimeters). In the following section, pre- and postreaction SEM-BSE images and EDS measurements are employed to probe the impact of transport at scales that are relevant to reactive processes (micrometers) to elucidate the interplay between spatial chemical heterogeneity and topological changes of the reacting interface.

Static Results. Fig. 4 shows the prereaction SEM-BSE photomicrographs, with areas of interest highlighted in blue boxes (Fig. 4*A*), prereaction composite elemental maps compiled using SEM-BSE and EDS data for the select region (Fig. 4*B*), postreaction SEM-BSE images of the same regions (Fig. 4*C*), and corresponding postreaction composite elemental maps (Fig. 4*D*). Full-scale SEM-BSE and EDS images showing all four quadrants are included in *SI Appendix*, Figs. S4–S7. These image files as well as individual elemental maps are provided in the Stanford Digital Repository.

Carbonate-poor samples. For the carbonate-poor samples (WC 3-2V and WC 6-1H; 8 and 21 wt %, respectively), small calcite (red) and dolomite (purple) particles are distributed throughout as apparent in the prereaction EDS images (Fig. 4*B*). Although no large-scale topological alterations are detected from the dynamic image analysis (as discussed in the previous section), surface carbonates dissolve when reactive fluids come in contact with the fracture surface. Dissolution continues until a reacted zone forms on and adjacent to the fracture walls, creating micrometer-sized (∼1- to 10-μm) moldic pores that correspond to dissolved calcite and dolomite grains (Fig. 4 *B* and *C*). This results in topological alterations of the physical interface that are undetected at a larger imaging scales (e.g., in the optical images), while its chemical composition is altered at the micrometer scale through the formation of a reacted interface zone. Fig. 4 shows that, in the WC 6-1H sample, the pores created adjacent to the surface are due to dissolution of calcite and dolomite, while further from the surface, only calcite grains dissolved. This result indicates that different reactivity rates between minerals may create a layered structure, which should be taken into account in reactive transport studies. Comparing WC 3-2V and WC 6-1H samples with the samples with intermediate carbonate content (WC 2-5H), WC 2-5H shows larger moldic pores and pathways where elongated fossils dissolved, while the former samples contain small, isolated moldic pores only. In addition to the generation of moldic micropores

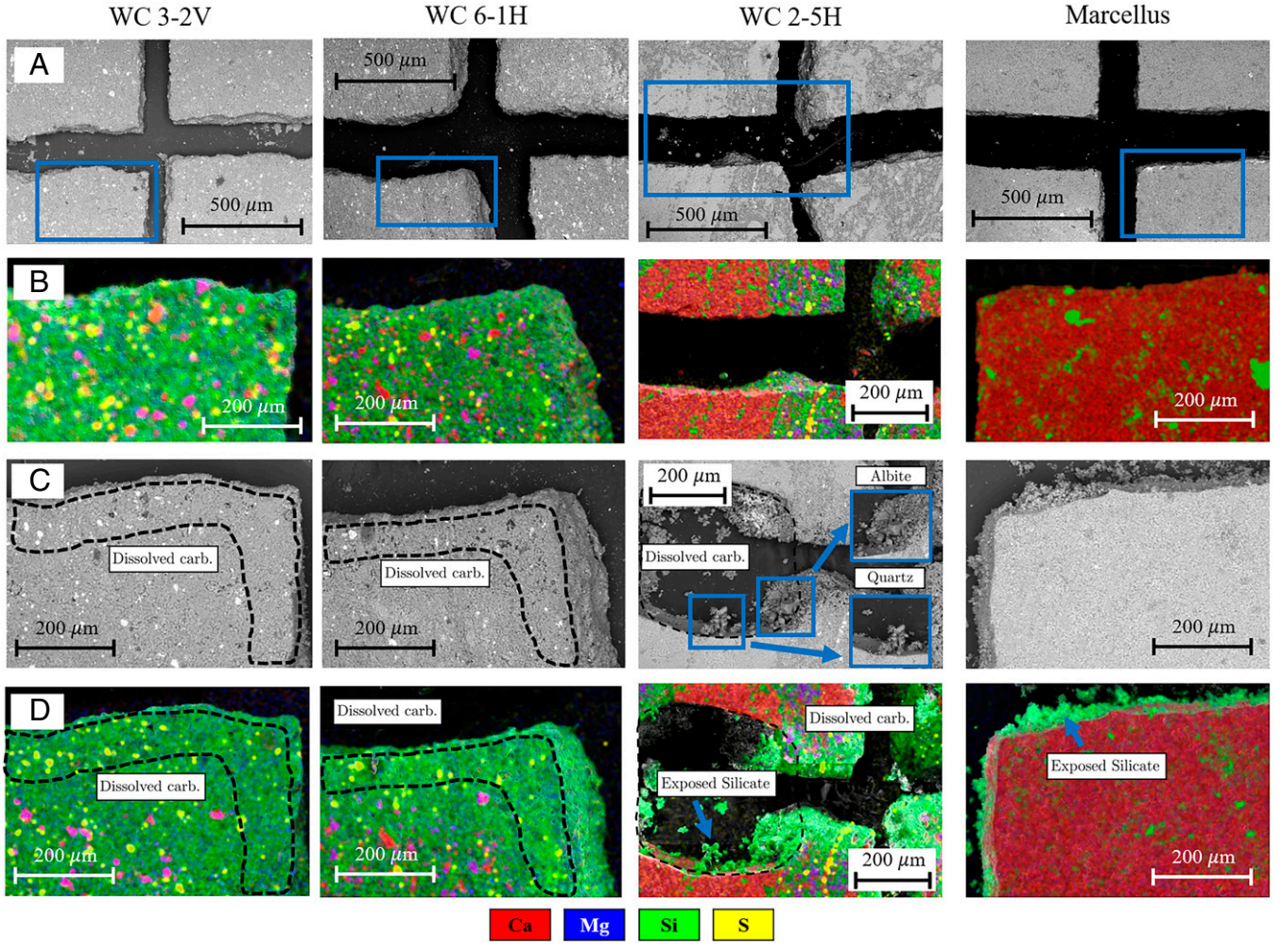

Fig. 4. (*A*) Prereaction SEM-BSE images of the four samples (image width = 1.38 mm). Blue boxes (image width ∼0.5 mm) correspond to select regions of prereaction EDS, postreaction SEM-BSE, and postreaction EDS images in *B*–*D*. (*B*) Prereaction composite elemental maps for the select region. (*C*) Postreaction SEM-BSE images of the same region. Insets show albite and quartz crystals exposed after the dissolution of surrounding calcite. (*D*) Corresponding postreaction composite elemental maps. Samples are ordered from carbonate-poor on the left to carbonate-rich on the right. The carbonate dissolution zones with newly developed porosity are indicated by dashed lines. The dashed region for WC 2-5H corresponds to calcite dissolved from both sides of the fracture. In this sample, calcite dissolution exposed euhedral quartz and albite. Fine-grained silicates are also exposed by calcite dissolution in the Marcellus sample. The colors indicate individual elements as listed for each composite element image. Full-size composite elemental images and SEM-BSE images are in *SI Appendix*, Fig. S4–S7. These images along with single element maps are available in the Stanford Digital Repository (see *Data Availability*).

shown in Fig. 4, substantial changes in the width, shape, and tortuosity of the fractures are caused by dissolution as the size of calcite and dolomite particles increases.

Samples with intermediate carbonate content. The heterogeneous WC 2-5H sample (65 wt % carbonate) contains mainly calcite as fossils (red in Fig. 4*B*) with dolomite (purple) locally distributed in silicate-rich (green) regions. Relatively nonreactive minerals formerly embedded within the calcite matrix are exposed by dissolution, including quartz, albite, and other silicates (green in Fig. 4*D*). The morphology of these grains range from euhedral to subhedral (Fig. 4*C*, *Insets*). In the WC 2-5H samples, compositional heterogeneities are reflected in the dissolution patterns. During reactive flow, the heterogeneous distribution of calcite in WC 2-5H leads to a significant macroscopic alteration of the fracture profile as indicated by the dashed regions in Fig. 4*C* for the sample. This is consistent with an increase in the interface area as dissolution proceeds, as highlighted by the positive correlations between Ψ and Γ, measured using dynamic image analysis (Fig. 3*B*). This affects subsequent reactive flow and transport processes as documented in the dynamic image data. Additionally, by comparing the pre- and postreaction samples saturated with dye and their processed equivalents (Fig. 3*A*), a sliver of nonreactive matrix that was attached to the elongated calcite fossil remains unsupported and potentially movable after the fossil dissolved. This suggests that large unreacted grains may be mobilized as a result of differential dissolution. Moreover, the WC 2-5H samples have a greater solid–fluid interface during the dissolution at both the fracture (Fig. 3) and pore (Fig. 4) scales. Additionally, in the WC 2-5H samples, the nonreactive portion consisting of silicates and organic matter is heterogeneously distributed. The greater continuity of the nonreactive silicates requires more extensive calcite dissolution to allow particles to be exposed to the fluid and potentially mobilized.

Carbonate-rich samples. In the carbonate-rich samples (Marcellus, 86 wt %), calcite (red) and minor amounts of silicate minerals (green) are homogeneously distributed (Fig. 4*B*). Unlike the other three samples, the carbonate-rich Marcellus sample does not exhibit a defined altered zone (Fig. 4*C*, Marcellus row). When dissolution occurs, the reaction is concentrated along the entire fracture surface, and moldic pores and elongated pathways do not form as in other samples. Instead, SEM results show that dissolution at the fracture surface in the carbonate-rich Marcellus sample uniformly reduces the length of the solid–fracture interface, therefore leading to negative $\Gamma - \Psi$ correlations as dissolution proceeds (Fig. 3*B*). In the postreaction composite EDS image, silicate minerals (green) are uniformly exposed on the fracture wall by dissolution of the surrounding calcite (red in Fig. 4*D*). These nonreactive particles remained attached to and/or are embedded in the fracture surface.

Implications for Reactive Transport Modeling and Reactivity Assessment. The unique ability to combine SEM-BSE and EDS images of the same sample pre- and postreaction, as well as in operando time-resolved optical measurements during dissolution, provides the opportunity to quantify the impact of carbonates spatial heterogeneity and their accessibility to connected pore space on reaction rates at a given flow rate. Quantitative estimates of the temporal evolution of mineral surface area in terms of porosity are at the foundation of a number of broadly used reactive transport codes, such as CrunchFlow, where reactivity is expressed in terms of a single value of mineral reactive surface area, A:

$$R = Akf_e,$$

where k is the reaction rate constant and f_e is a function of Gibbs free energy or the thermodynamic driving force (16). Discrepancies between mineral dissolution rates observed in laboratory experiments vs. natural samples have been attributed, among others, to porous medium effects, where the accessibility of reactive mineral surfaces (e.g., carbonates) may be strongly controlled by their spatial distribution relative to the connected pore structure (16). For real rock samples, the assumption that A is the same as that of the pure reactive substance may require adjustments by scaling factors of various orders of magnitude ($10^{-3} - 10^{-1}$). A number of studies have emphasized the difficulty in estimating and constraining the reactive surface area for reactive transport codes (16, 17). Geometry-based methods are widely applied where minerals are assumed to have simple geometries. As a result, during dissolution processes, the temporal evolution of mineral surface area is generally captured through (equation 2 in ref. 17)

$$A(t) = A^i \left(\frac{\phi_m(t)}{\phi_m^i}\right)^{\frac{2}{3}} \left(\frac{\phi(t)}{\phi^i}\right)^{\frac{2}{3}},$$

where ϕ_m is the reactive mineral volume fraction and ϕ is the porosity. The superscript "i" refers to the corresponding quantity evaluated at $t = 0$. For the set of experiments with Marcellus samples (high carbonate content), $\phi_m(t)$ can be approximated as $\phi_m(t) \approx \phi^e - \phi(t)$, where ϕ^e is the porosity evaluated at the end of the experiment $\phi^e = \phi(t_{end})$. Then, the previous model can be recast in terms of Γ and Ψ as follows:

$$\Gamma(t) = \left(\frac{\Psi(t_{end}) - \Psi(t)}{\Psi(t_{end}) - 1}\right)^{\frac{2}{3}} \Psi(t)^{\frac{2}{3}}$$

since $\Gamma(t) = A(t)/A^i$ and $\Psi(t) = \phi(t)/\phi^i$, when the sample is quasi-2D. This leads to the following scaling relationship:

$$\Gamma \sim -\Psi^{\frac{4}{3}}. \qquad \textbf{[1]}$$

Fig. 3*B* shows that Eq. **1** (dashed blue line) correctly captures the experimental trend for the Marcellus samples, in which 1) an increase in porosity leads to a decrease in surface area (due to grains becoming more rounded as dissolution progresses) and 2) there is no limitation in reactive area accessibility to the fracture network, where the acid flows (i.e., porous media effects are negligible). This result also shows that, in this setup, three-dimensional effects can be neglected to leading order when estimating $A - \phi$ trends. Instead, for WC 2-5H samples (as well as for low-carbonate samples), the correlation between Γ and Ψ significantly deviates from Eq. **1**; from the experiments on WC 2-5H samples, a scaling relationship of $\Gamma \sim \Psi^{1/2}$ (dashed red line) can be extracted (where Γ now refers to the total surface area). Such a scaling is able to capture an increase in surface area during dissolution due to surface roughening caused by the spatial distribution of carbonate inclusions as well as their limited accessibility to the fracture network, where acid is flowing. However, more complex correlations may be warranted to account for additional effects (e.g., achievement of a plateau at finite times). Scaling laws that deviate from those theoretically predicted by Eq. **1** can be traced back to the highly nonlinear temporal evolution of both surface area and fracture volume during dissolution, as shown in *SI Appendix*, Fig. S18, compared with a linear behavior observed in the Marcellus samples. Such nonlinearities can be primarily attributed to accessibility limitations of reactive surfaces to the connected pore space (i.e., to the spatial distribution and characteristic size of carbonate inclusions, which in turn, are a function of carbonate content). These observations suggest that, for these samples, carbonate content can be used as an a priori proxy to assess the potential impact of porous medium effects on

reactive transport rates at a fixed flow rate. This analysis shows how the experimental framework developed in this work can 1) be directly used to constrain $A - \phi$ correlations in reactive transport models (at fixed flow rate) and 2) inform the development of dynamic correlations for natural samples with different compositions, in which porous medium effects become predominant due to the spatial heterogeneity of reactive minerals and their accessibility to the connected pore structure. Note that the combination of optical measurements with compositional analysis enables us, on the one hand, to extract $A - \phi$ correlations based on total surface area (rather than reactive area), therefore potentially simplifying image analysis, and, on the other hand, to perform a more detailed analysis tracking specific minerals.

Conclusions

We investigated dissolution of real geological samples using our microfluidic experimental platform that allows for static characterization at the micro- and submicrometer scales and dynamic characterization at the millimeter scale.

We tested eight (including four repeat experiments) shale samples with a range of reactive mineral concentrations and microstructures. We injected 1% HCl as an acidic fluid. We conducted SEM imaging to characterize the static pre- and postreaction samples and collected EDS data to detect changes in composition before and after dissolution. All of the prereaction, concurrent, and postreaction measurements were correlated to achieve detailed characterization of the same regions of interest at different scales ranging from the millimeter scale to the micrometer scale. This protocol allows us to trace accurately dissolution of calcite and dolomite, exposure of nonreactive particles, structural changes at the fracture and pore scales, solid–fracture interface and fracture volume trends, and mineral compositions at the same locations.

For samples with less than 30 wt % carbonate (WC 3-2V and WC 6-1H), reactive minerals (calcite and dolomite) are present as small grains and distributed homogeneously throughout the entire sample. Although their dissolution leaves small moldic pores in the matrix ($\sim$1 to 100 μm), the matrix does not lose its integrity because of the presence of supporting silicates; as a result, the fracture geometry remains unaffected at the millimeter scale, leading to constant values of fracture volume and interface area during the dissolution process. For the samples with intermediate carbonate content (65 wt %), reactive calcite occurs as large particles that are distributed heterogeneously. When exposed to reactive fluids, large voids develop as the calcite is selectively dissolved. This leads to an increase in fracture surface and volume as dissolution proceeds (i.e., in positive fracture–surface vs. fracture–volume correlations in Fig. 3*B*). For the carbonate-rich Marcellus samples, fracture volume increases due to the uniform widening of preexisting fractures, which also reduces the overall interface length, leading to negative fracture–surface vs. fracture–volume correlations as dissolution proceeds. These observations are critical to assess the temporal scales of natural dissolution and optimize geological engineering applications. The high–temporal resolution data, combined with compositional analysis, provide a workflow for estimating reactivity of real rock samples by quantifying the temporal correlation between surface area and pore volume during dissolution. Specifically, deviations from theoretically postulated correlations can be quantified and traced back to the temporally nonlinear evolution of surface area and fracture porosity during dissolution for samples in which intermediate carbonate content and its heterogeneous distribution translate into limitations in reactive surface accessibility to the connected pore space (i.e., significant porous media effects).

Additionally, the use of both dynamic and static measurements shows that nonreactive particles are exposed at different rates, depending on their composition, distribution, the fracture volume, and the solid–fluid interface length behavior as dissolution progresses. These data show different possible mechanisms associated with exposure of unreacted fines: 1) constant exposure of small nonreactive particles embedded in the calcite matrix (Fig. 4*D*, Marcellus) and 2) dissolution of large calcite particles, which could lead to weakening and mobilization of portions of the matrix itself (Figs. 3*A* and 4*D*, WC 2-5H). In particular, the dynamic results suggest that small particles are exposed constantly during dissolution of the carbonate-rich sample. The matrix weakening requires longer exposure times and results in significant changes of the fracture structure, and it may cause fracture collapse for heterogeneous samples with intermediate carbonate content. It is worth pointing out that the presence of nonreactive particles was detected both in the effluent as well as on the PDMS surface, in the proximity of the fracture surface, after dissolution. This suggests that, at this Péclet number, dissolution-driven mechanical erosion (i.e., loosening of particles and entertainment by the flow) may lead to nonreactive particle displacement and consequent pore clogging.

Our study demonstrates the potential and multifunctional nature of this sample-embedded microfluidics platform for studying the dynamics of geochemical reactions and its direct application to constrain reactive transport models by extracting a relationship $\Gamma \sim f(\Psi)$ using high–temporal resolution data. Also, the ability to track in time, at high temporal resolution, the evolution of (and correlation between) fracture volume and solid–fracture interface length might prove very insightful in the identification and quantification of (precursors of) instabilities (i.e., wormholes) as well as other complex feedbacks between mineral dissolution, flow, and transport under different dynamic conditions (i.e., *Pe*). The combination of static and dynamic measurements on the sample allows one to explore the mechanisms and the synergy of reactive transport, flow, and geochemistry at multiple scales.

Data Availability. Optical and SEM images have been deposited in the Stanford Digital Repository (43). All other study data are included in the article and/or *SI Appendix*.

ACKNOWLEDGMENTS. This work was supported as part of the Center for Mechanistic Control of Unconventional Formations, an Energy Frontier Research Center funded by US Department of Energy, Office of Science, Basic Energy Sciences Award DE-SC0019165. Part of this work was performed at the Stanford Nano Shared Facilities supported by NSF Award ECCS-2026822.

Author affiliations: [a]Energy Resources Engineering, Stanford University, Stanford, CA 94305; and [b]Stanford Synchrotron Radiation Lightsource, SLAC National Accelerator Laboratory, Menlo Park, CA 94025

1. M. L. Frezzotti, J. Selverstone, Z. D. Sharp, R. Compagnoni, Carbonate dissolution during subduction revealed by diamond-bearing rocks from the Alps. *Nat. Geosci.* **4**, 703–706 (2011).
2. O. Sulpis, B. P. Boudreau, A. Mucci, C. Jenkins, R. M. Key, Current $CaCO_3$ dissolution at the seafloor caused by anthropogenic CO_2. *Proc. Natl. Acad. Sci. U.S.A.* **115**, 11700–11705 (2018).
3. J. P. Fitts, C. A. Peters, Caprock fracture dissolution and CO_2 leakage. *Rev. Mineral. Geochem.* **77**, 459–479 (2013).
4. A. L. Harrison *et al.*, Element release and reaction-induced porosity alteration during shale-hydraulic fracturing fluid interactions. *Appl. Geochem.* **82**, 47–62 (2017).
5. C. Noiriel, B. Madé, P. Gouze, Impact of coating development on the hydraulic and transport properties in argillaceous limestone fracture. *Water Resour. Res.* **43**, W09406 (2007).
6. C. Wang *et al.*, An invisible soil acidification: Critical role of soil carbonate and its impact on heavy metal bioavailability. *Sci. Rep.* **5**, 12735 (2015).
7. M. Konrad-Schmolke *et al.*, Mineral dissolution and reprecipitation mediated by an amorphous phase. *Nat. Commun.* **9**, 1637 (2018).
8. B. R. Ellis *et al.*, Dissolution-driven permeability reduction of a fractured carbonate caprock. *Environ. Eng. Sci.* **30**, 187–193 (2013).

9. B. Grieser, B. Wheaton, B. Magness, M. Blauch, R. Loghry, "Surface reactive fluid's effect on shale" Paper presented at the *SPE Production and Operations Symposium* held in Oklahoma City, OK, (2007). https://doi.org/10.2118/106815-MS. Accessed 27 July 2022.
10. H. Aljamaan, C. M. Ross, A. R. Kovscek, Multiscale imaging of gas storage in shales. *SPE J.* **22**, 1760–1777 (2017).
11. Y. Gensterblum *et al*., Gas transport and storage capacity in shale gas reservoirs: A review. Part A, Transport processes. *J. Unconv. Oil Gas Resour.* **12**, 87–122 (2015).
12. K. S. Lee, T. H. Kim, *Transport in Shale Reservoirs* (Gulf Professional Publishing, Cambridge, United Kingdom, 2019).
13. S. S. Morsy, J. J. Sheng, M. Y. Soliman, "Improving hydraulic fracturing of shale formations by acidizing" Paper presented at the *SPE Eastern Regional Meeting* held in Pittsburgh, PA, (2013). https://doi.org/10.2118/165688-MS. Accessed 27 July 2022.
14. J. A. Hakala *et al*., "Laboratory-scale studies on chemical reactions between fracturing fluid and shale core from the Marcellus Shale Energy and Environmental Laboratory (MSEEL) site" Paper presented at the SPE/AAPG/SEG *Unconventional Resources Technology Conference* held in Austin, TX, (2017). https://doi.org/10.15530/URTEC-2017-2670856. Accessed 27 July 2022.
15. Q. Li, A. D. Jew, G. E. Brown Jr., J. R. Bargar, K. Maher, Reactive transport modeling of shale–fluid interactions after imbibition of fracturing fluids. *Energy Fuels* **34**, 5511–5523 (2020).
16. L. E. Beckingham *et al*., Evaluation of mineral reactive surface area estimates for prediction of reactivity of a multi-mineral sediment. *Geochim. Cosmochim. Acta* **188**, 310–329 (2016).
17. F. Qin, L. E. Beckingham, The impact of mineral reactive surface area variation on simulated mineral reactions and reaction rates. *Appl. Geochem.* **124**, 104852 (2021).
18. V. Vishal *et al*., Interpreting pore dimensions in gas shales using a combination of SEM imaging, small-angle neutron scattering, and low-pressure gas adsorption. *Energy Fuels* **33**, 4835–4848 (2019).
19. Y. Zhang, T. J. Barber, Q. Hu, M. Bleuel, H. F. El-Sobky, Complementary neutron scattering, mercury intrusion and SEM imaging approaches to micro- and nano-pore structure characterization of tight rocks: A case study of the Bakken shale. *Int. J. Coal Geol.* **212**, 103252 (2019).
20. L. Frouté, A. R. Kovscek, "Nano-imaging of shale using electron microscopy techniques" Paper presented at the SPE/AAPG/SEG *Unconventional Resources Technology Conference*, virtual (2020). https://doi.org/10.15530/urtec-2020-3283. Accessed 27 July 2022.
21. C. J. Werth, C. Zhang, M. L. Brusseau, M. Oostrom, T. Baumann, A review of non-invasive imaging methods and applications in contaminant hydrogeology research. *J. Contam. Hydrol.* **113**, 1–24 (2010).
22. D. C. Joy, Scanning electron microscopy for materials characterization - sciencedirect. *Curr. Opin. Solid State Mater. Sci.* **2**, 465–468 (1997).
23. C. Soulaine, S. Roman, A. Kovscek, H. A. Tchelepi, Mineral dissolution and wormholing from a pore-scale perspective. *J. Fluid Mech.* **827**, 457–483 (2017).
24. H. Yoon, K. N. Chojnicki, M. J. Martinez, Pore-scale analysis of calcium carbonate precipitation and dissolution kinetics in a microfluidic device. *Environ. Sci. Technol.* **53**, 14233–14242 (2019).
25. J. Poonoosamy *et al*., A microfluidic experiment and pore scale modelling diagnostics for assessing mineral precipitation and dissolution in confined spaces. *Chem. Geol.* **528**, 119264 (2019).
26. W. Song, F. Ogunbanwo, M. Steinsbø, M. A. Fernø, A. R. Kovscek, Mechanisms of multiphase reactive flow using biogenically calcite-functionalized micromodels. *Lab Chip* **18**, 3881–3891 (2018).
27. D. Ross, R. M. Bustin, The importance of shale composition and pore structure upon gas storage potential of shale gas reservoirs. *Mar. Pet. Geol.* **26**, 916–927 (2009).
28. T. Saif, Q. Lin, A. R. Butcher, B. Bijeljic, M. J. Blunt, Multi-scale multi-dimensional microstructure imaging of oil shale pyrolysis using X-ray micro-tomography, automated ultra-high resolution SEM, MAPS mineralogy and FIB-SEM. *Appl. Energy* **202**, 628–647 (2017).
29. D. M. Wang, Y. M. Xu, D. M. He, J. Guan, O. M. Zhang, Investigation of mineral composition of oil shale. *Asia-Pac. J. Chem. Eng.* **4**, 691–697 (2009).
30. G. Kosakowski, B. Berkowitz, Flow pattern variability in natural fracture intersections. *Geophys. Res. Lett.* **26**, 1765–1768 (1999).
31. A. Dahi Taleghani, J. E. Olson, How natural fractures could affect hydraulic-fracture geometry. *SPE J.* **19**, 161–171 (2013).
32. O. Kolawole, I. Ispas, Interaction between hydraulic fractures and natural fractures: Current status and prospective directions. *J. Pet. Explor. Prod. Technol.* **10**, 1613–1634 (2020).
33. J. F. W. Gale, S. E. Laubach, J. E. Olson, P. Eichhubl, A. Fall, Natural fractures in shale: A review and new observations. *AAPG Bull.* **98**, 2165–2216 (2014).
34. H. Wen, L. Li, D. Crandall, A. Hakala, Where lower calcite abundance creates more alteration: Enhanced rock matrix diffusivity induced by preferential carbonate dissolution. *Energy Fuels* **30**, 4197–4208 (2016).
35. H. Fazeli, M. Nooraiepour, H. Hellevang, Microfluidic study of fracture dissolution in carbonate-rich caprocks subjected to CO_2 -charged brine. *Ind. Eng. Chem. Res.* **59**, 450–457 (2019).
36. H. Deng, J. P. Fitts, R. V. Tappero, J. J. Kim, C. A. Peters, Acid erosion of carbonate fractures and accessibility of arsenic-bearing minerals: In operando synchrotron-based microfluidic experiment. *Environ. Sci. Technol.* **54**, 12502–12510 (2020).
37. C. T. Gerold, A. T. Krummel, C. S. Henry, Microfluidic devices containing thin rock sections for oil recovery studies. *Microfluid. Nanofluidics* **22**, 76 (2018).
38. M. Nooraiepour, H. Fazeli, R. Miri, H. Hellevang, Effect of CO_2 phase states and flow rate on salt precipitation in shale caprocks–a microfluidic study. *Environ. Sci. Technol.* **52**, 6050–6060 (2018).
39. C. Zhang, M. Oostrom, T. W. Wietsma, J. W. Grate, M. G. Warner, Influence of viscous and capillary forces on immiscible fluid displacement: Pore-scale experimental study in a water-wet micromodel demonstrating viscous and capillary fingering. *Acta Ophthalmol.* **25**, 3493–3505 (2011).
40. B. Ling, H. J. Khan, J. L. Druhan, I. Battiato, Multi-scale microfluidics for transport in shale fabric. *Energies* **14**, 21 (2020).
41. B. Ling, J. Bao, M. Oostrom, I. Battiato, A. M. Tartakovsky, Modeling variability in porescale multiphase flow experiments. *Adv. Water Resour.* **105**, 29–38 (2017).
42. S. Molins *et al*., Simulation of mineral dissolution at the pore scale with evolving fluid-solid interfaces: Review of approaches and benchmark problem set. *Comput. Geosci.* **25**, 1285–1318 (2021).
43. B. Ling *et al*., Image supplement for "Probing multiscale dissolution dynamics in natural rocks through microfluidics and compositional analysis." Stanford Digital Repository. https://purl.stanford.edu/fc236gc0777. Deposited 14 July 2022.